Trap and Transfer. Two-Step Hole Injection Across the Sb_2S_3/CuSCN Interface in Solid-State Solar Cells

Jeffrey A. Christians[†] and Prashant V. Kamat[†,‡,*]

Radiation Laboratory, [†]Department of Chemical and Biomolecular Engineering, and [‡]Department of Chemistry and Biochemistry, University of Notre Dame, Notre Dame, Indiana 46556, United States

ABSTRACT In solid-state semiconductor-sensitized solar cells, commonly known as extremely thin absorber (ETA) or solid-state quantum-dot-sensitized solar cells (QDSCs), transfer of photogenerated holes from the absorber species to the p-type hole conductor plays a critical role in the charge separation process. Using Sb_2S_3 (absorber) and CuSCN (hole conductor), we have constructed ETA solar cells exhibiting a power conversion efficiency of 3.3%. The hole transfer from excited Sb_2S_3 into CuSCN, which limits the overall power conversion efficiency of these solar cells, is now independently studied using transient absorption spectroscopy. In the Sb_2S_3 absorber layer, photogenerated holes are rapidly localized on the sulfur atoms of the crystal lattice, forming a sulfide radical ($S^{-\bullet}$) species. This trapped hole is transferred from the Sb_2S_3 absorber to the CuSCN hole conductor with an exponential time constant of 1680 ps. This process was monitored through the spectroscopic signal seen for the $S^{-\bullet}$ species in Sb_2S_3, providing direct evidence for the hole transfer dynamics in ETA solar cells. Elucidation of the hole transfer mechanism from Sb_2S_3 to CuSCN represents a significant step toward understanding charge separation in Sb_2S_3 solar cells and provides insight into the design of new architectures for higher efficiency devices.

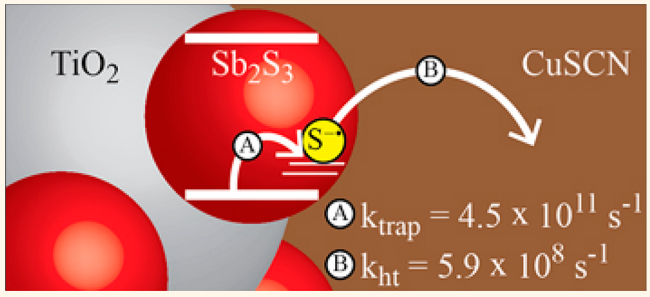

KEYWORDS: photovoltaics · Sb_2S_3 · CuSCN · transient absorption spectroscopy · extremely thin absorber · quantum dots · solid-state solar cells · hole transfer

Sensitized solar cells (SSCs) show promise for the next generation of photovoltaics due to the possibility of lower production costs compared to current commercial crystalline and polycrystalline p–n junction photovoltaics.[1,2] SSCs employ a wide band gap semiconductor which is sensitized for light absorption using a semiconductor (extremely thin absorber, ETA solar cells, and quantum-dot-sensitized solar cells, QDSCs) or an organic dye (dye-sensitized solar cells, DSSCs). The working mechanism for all classes of solar cells is the separation of photogenerated electron–hole pairs before recombination takes place. In current commercial photovoltaics, this separation is achieved *via* an internal electric field generated by the junction of a p-type and n-type semiconductor, such as doped silicon.[3] However, in SSCs, the nanocrystals used are too small to support a significant electric field.[4] These solar cells achieve charge separation through the injection of electrons from the thin absorber layer into an electron acceptor (generally TiO_2) and holes into a hole acceptor (generally a liquid redox couple electrolyte).[1,4] By removing electrons and holes from the absorber layer and separating them spatially, electron–hole recombination is reduced as are the quality requirements for the solar cell materials, opening up new possibilities for low-cost photovoltaics.[5,6] Despite the promise of low-cost SSC production, recent efforts to commercialize liquid-junction DSSCs have revealed difficulties in sealing the liquid electrolyte to prevent evaporation and leakage.[7–9] For this reason, there has been much interest in developing solid-state SSCs that are able to compete commercially;[10] however, current efficiencies of solid-state devices remain low compared to other photovoltaic technologies.[11]

Semiconductor quantum dots (QDs) have a variety of properties that make them promising candidates for high-efficiency

* Address correspondence to pkamat@nd.edu.

Received for review June 17, 2013 and accepted August 15, 2013.

Published online August 15, 2013
10.1021/nn403058f

solid-state QDSCs and ETA solar cells. They offer a tunable band gap and band edge through size quantization,[12] large intrinsic dipole moments,[13] and high extinction coefficients.[14] They also open up the possibility of surpassing the theoretical efficiency of p–n junction solar cells imposed by the Shockley–Queisser limit through hot electron injection[15] and multiple exciton generation.[16,17] A variety of semiconductors have been explored for use in these solar cells, including CdS,[18] CdSe,[19–21] In_2S_3,[22] and Sb_2S_3.[23–29] Among these, Sb_2S_3 ETA solar cells employing CuSCN as the hole conductor show good air stability,[25] and efficiencies have been reported of 3–4% under full sun illumination.[9,25,26,28] In addition, crystalline Sb_2S_3 (stibnite) has a band gap of 1.7–1.8 eV,[30] allowing for light absorption throughout the visible range, and CuSCN has high p-type conductivity of 10^{-2} to 10^{-3} Ω^{-1} cm^{-1},[31] indicating that even higher efficiencies are realizable using these materials.[9]

These previous studies show the potential for Sb_2S_3/CuSCN ETA solar cells as the next generation of inexpensive photovoltaics. However, a better understanding of the charge separation process is required to expedite the development of higher efficiency devices. In the present study, transient absorption spectroscopy is employed to elucidate the dynamics of the photogenerated holes.[32–34] The hole trapping in the Sb_2S_3 and transfer from Sb_2S_3 to CuSCN is investigated by following the spectroscopic signals arising from photogenerated holes in Sb_2S_3 ($S^{-\bullet}$ radical). These experiments provide a further understanding of the charge separation mechanism in Sb_2S_3 ETA solar cells and highlight several possible strategies for improving photovoltaic performance.

RESULTS AND DISCUSSION

Photovoltaic Performance. Solid-state solar cells using an Sb_2S_3 absorber and CuSCN hole conductor were fabricated using similar methods as discussed previously in the literature.[9,25] A schematic of a fully fabricated solar cell alongside a cross sectional SEM image is shown in Figure 1A, B. The light energy conversion efficiency of these solar cells was determined from current–voltage (J–V) and incident photon to carrier efficiency (IPCE) measurements obtained following a 2 h light soaking period. J–V characteristics under AM 1.5G simulated solar irradiation are presented in Figure 2A, and the short-circuit current density (J_{SC}), open-circuit voltage (V_{OC}), fill factor (ff), and power conversion efficiency (η) of the TiO_2/Sb_2S_3/CuSCN solar cell were 12.4 mA cm^{-2}, 455 mV, 0.59, and 3.3%, respectively. The IPCE spectrum seen in Figure 2B shows photocurrent generation across the visible spectrum with a peak external quantum efficiency (EQE) of 73% at 500 nm.

These solid-state antimony sulfide ETA solar cells show good stability,[25] eliminate the electrolyte leakage issues seen in liquid-junction solar cells, and exhibit promising power conversion efficiencies; however, in order to make ETA solar cells practically viable, one needs to further improve

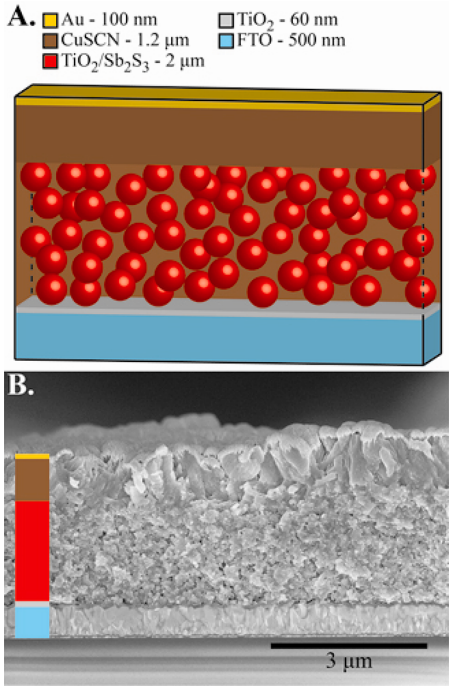

Figure 1. (A) Scheme of TiO_2/Sb_2S_3/CuSCN solar cell showing approximate thicknesses of each layer as measured by SEM. (B) SEM cross section image of a TiO_2/Sb_2S_3/CuSCN solar cell.

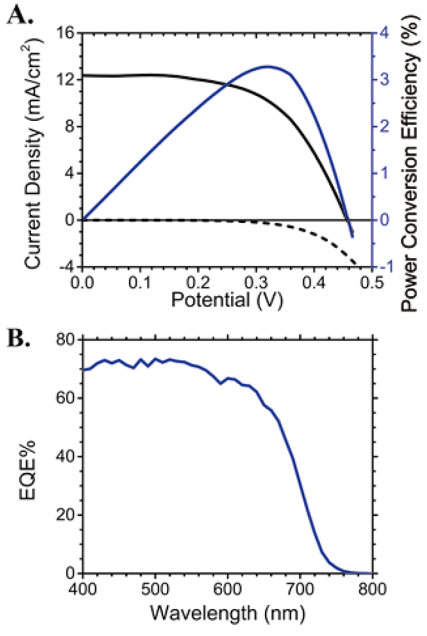

Figure 2. (A) J–V characterization at 1 sun illumination (solid) and in the dark (dashed) shown in black (left ordinate) and power conversion efficiency shown in blue (right ordinate) of TiO_2/Sb_2S_3/CuSCN solar cell. (B) IPCE spectrum showing peak external quantum efficiency of 73% at 500 nm. Solar cell active area was masked to be 0.1 cm^2.

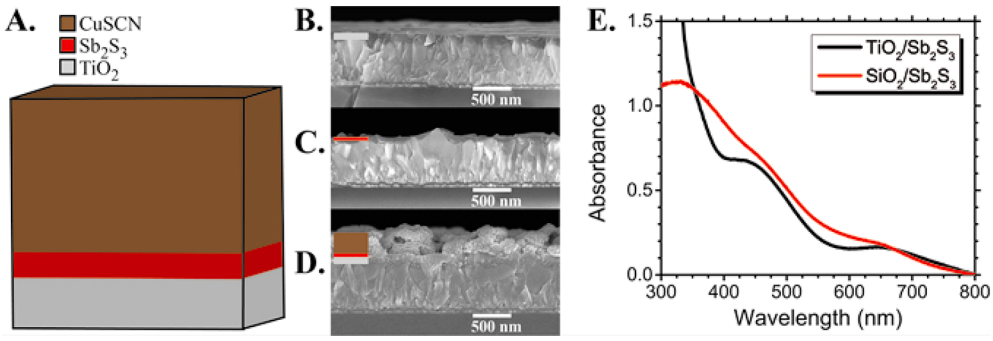

Figure 3. (A) Scheme of planar TiO_2/Sb_2S_3/CuSCN films used in transient absorption spectroscopy showing approximate thicknesses of each layer as measured by SEM. SEM cross section images of (B) compact TiO_2 layer on FTO, (C) Sb_2S_3 layer on FTO, and (D) completed TiO_2/Sb_2S_3/CuSCN film. Films were deposited on FTO glass for imaging purposes, and film D was coated with 2.5 nm of Au *via* sputtering. (E) UV−visible absorption spectrum of a TiO_2/Sb_2S_3 and SiO_2/Sb_2S_3 films with 42 and 47 nm thick Sb_2S_3 layer, respectively, used in transient absorption spectroscopy studies.

the efficiency. A basic understanding of the limiting factors is necessary for further improvement in solar cell performance.

Steady-State Sb_2S_3 Film Characterization. To investigate the charge transfer dynamics of the TiO_2/Sb_2S_3/CuSCN system, four different layered films were constructed: (A) TiO_2/Sb_2S_3, (B) TiO_2/Sb_2S_3/CuSCN, (C) SiO_2/Sb_2S_3, and (D) SiO_2/Sb_2S_3/CuSCN. A diagram and SEM cross sectional images of a TiO_2/Sb_2S_3/CuSCN film are shown in Figure 3A−D. Unlike the mesoporous films used for high-efficiency solar cells, Sb_2S_3 was deposited on a planar nonporous TiO_2 or SiO_2 layer. TiO_2 films were deposited on cleaned glass microscope slides by spray pyrolysis,[35] and cleaned glass slides were used as SiO_2 films. These two metal oxide substrates were chosen because TiO_2 accepts photoelectrons from Sb_2S_3 while SiO_2 does not. Planar metal oxide substrates were used to allow precise control of the Sb_2S_3 layer thickness and minimization of both light absorption and scattering. Amorphous Sb_2S_3 was deposited on the TiO_2 and SiO_2 substrates by chemical bath deposition and then annealed in nitrogen to obtain crystalline Sb_2S_3. Finally, CuSCN was deposited from a di-*n*-propyl sulfide solution using a homemade deposition apparatus. The thickness of the TiO_2 and CuSCN films was measured using SEM cross sectional analysis. Thickness of the Sb_2S_3 layer was determined using the absorption coefficient of the Sb_2S_3 films (eq 1).

$$A = \alpha \times d \quad (1)$$

where A is the absorbance of the film, α is the absorption coefficient of Sb_2S_3, and d is the average thickness of the film. To obtain a value for the absorption coefficient, UV−visible absorption measurements and SEM cross sectional analysis were conducted on Sb_2S_3 deposited on a fluorine-doped tin oxide (FTO) glass substrate. From these measurements, the absorption coefficient was calculated to be 1.5×10^5 cm^{-1} at 450 nm, a value consistent with previously reported measurements.[36,37] The

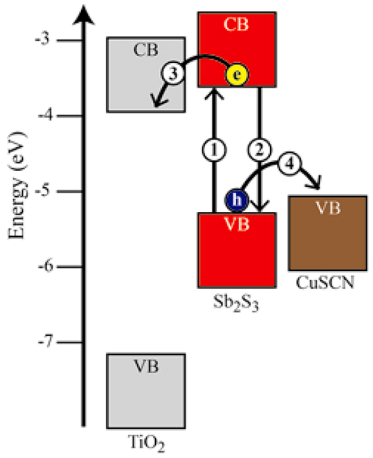

Figure 4. Energy level diagram of TiO_2/Sb_2S_3/CuSCN ETA solar cell[38] showing the four basic electron transfer reactions.

UV−visible absorption characteristics of films of Sb_2S_3 on TiO_2 and SiO_2 are shown in Figure 3E.

Transient Absorption Characterization. Transient absorption spectroscopy is a convenient tool for probing the recombination dynamics of semiconductors, which can be used to extract information on electron transfer reactions occurring in the system. Time-resolved transient spectra were recorded over a time window of 0−1500 ps following a 387 nm laser pulse on the four-layered Sb_2S_3 films described above: (A) TiO_2/Sb_2S_3, (B) TiO_2/Sb_2S_3/CuSCN, (C) SiO_2/Sb_2S_3, and (D) SiO_2/Sb_2S_3/CuSCN. In these films, four basic electron transfer reactions provide an outline for the overall exciton dynamics of the system. These electron transfer reactions can be understood using the band energy diagram seen in Figure 4. Following photoexcitation, an exciton is formed in Sb_2S_3 (reaction 2), giving rise to a photobleaching of the Sb_2S_3 absorbance. Because Sb_2S_3 is an indirect band gap semiconductor,[30] one pathway for this exciton to recombine is through nonradiative electron−hole recombination, resulting in the release of heat (reaction 3). The exciton can also decay through two charge transfer reactions, electron

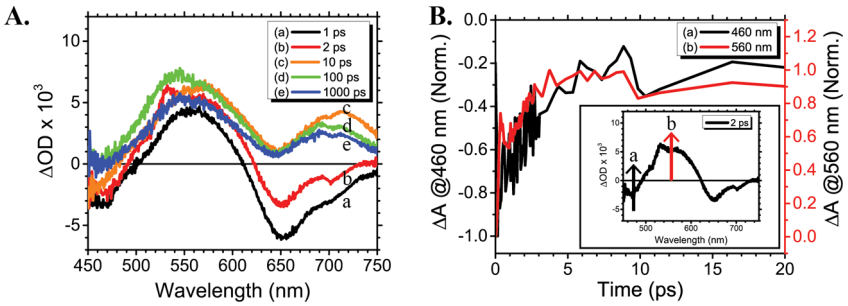

Figure 5. (A) Time-resolved transient spectra recorded after (a) 1 ps, (b) 2 ps, (c) 10 ps, (d) 100 ps, and (e) 1000 ps following a 387 nm laser pulse excitation of a TiO_2/Sb_2S_3 film in a vacuum. Other films studied show similar spectra; see Figure SI-1 in Supporting Information. (B) Transient kinetic trace of TiO_2/Sb_2S_3 film recorded at early times showing the correlation between (a) the relaxation kinetics observed at the 460 nm bleaching recovery (black/left ordinate) and (b) the rise time of the $S^{-\bullet}$ induced absorption at 560 nm (red/right ordinate). Inset shows the transient spectra recorded at 2 ps delay time to illustrate the wavelength at which these kinetic traces were monitored.

injection from Sb_2S_3 into TiO_2 (reaction 4) and hole injection from Sb_2S_3 into CuSCN (reaction 5).

$$Sb_2S_3 + h\nu \rightarrow Sb_2S_3(h + e) \quad (2)$$

$$Sb_2S_3(h + e) \rightarrow Sb_2S_3 + \text{heat} \quad (3)$$

$$Sb_2S_3(h + e) + TiO_2 \rightarrow Sb_2S_3(h) + TiO_2(e) \quad (4)$$

$$Sb_2S_3(h) + CuSCN \leftrightarrow Sb_2S_3 + CuSCN(h) \quad (5)$$

By analyzing the time-resolved difference absorption spectra, it is possible to evaluate these four reactions. Difference absorption reveals any changes in absorption, photobleaching ($\Delta A < 0$), or induced absorption ($\Delta A > 0$), associated with the formation of a transient state following laser pulse excitation (eq 6).

$$\Delta A = A_{(ES)} - A_{(GS)} \quad (6)$$

where $A_{(GS)}$ is the absorbance of the material in the ground state, and $A_{(ES)}$ is the absorbance of the excited state. In the absence of any electron acceptor or donor species, as in SiO_2/Sb_2S_3 films, the bleaching recovery reflects the relaxation of excited Sb_2S_3 to the ground state through recombination (reaction 3). Transfer of the electron or hole across a heterojunction (reactions 4 and 5) causes the photobleaching to recover faster, allowing for the calculation of the charge transfer kinetic rates. On the other hand, induced absorptions facilitate tracking the growth and decay of new species formed following excitation.[39]

The time-resolved difference absorption spectra recorded following 387 nm laser pulse excitation of TiO_2/Sb_2S_3 film are shown in Figure 5A. The time-resolved spectra exhibit two photobleaching maxima in the Sb_2S_3 absorbance at 650 and 460 nm and two induced absorption maxima at 560 and 725 nm. This spectral feature was observed in all Sb_2S_3 films (see Figure SI-1 in the Supporting Information). Analysis of the two induced absorption peaks at 560 and 725 nm reveals that these peaks have identical decay kinetics, as shown in Figure SI-2. This kinetic simultaneity indicates that the two induced absorption peaks arise from a single broad induced absorption feature which is convoluted with the photobleach seen at 650 nm. The bleaches in the Sb_2S_3 absorption at 650 and 460 nm are attributed to a photobleaching of the first and second excitonic peaks seen in the steady-state absorption of Sb_2S_3. The overlap of the induced absorption and 650 nm bleach complicates further analysis of the bleach recovery at this wavelength. Hence, further investigation was done using the bleach peak at 460 nm.

Hole Trapping *via* Transient Absorption. The induced absorption peak with maximum at 560 nm was assigned to the presence of $S^{-\bullet}$ or trapped holes in the Sb_2S_3. Previously, it has been confirmed *via* pulse radiolysis[40] and laser flash photolysis[41−44] that $S^{-\bullet}$ species formed in metal sulfide particles exhibit absorption features in the 450−650 nm region. This $S^{-\bullet}$ species is formed when valence band holes become localized on one of the Sb_2S_3 sulfur atoms (shown as $Sb_2S_2S^{-\bullet}$). Based on previous studies,[45] this sulfide radical is expected to form by trapping of the charge on the Sb_2S_3 surface, shown in reaction 7, giving rise to the observed $S^{-\bullet}$ induced absorption. However, Sb_2S_3 has an orthorhombic crystal structure with two distinct sulfur bonds, a strong short-range Sb−S bond and a weaker long-range bond provided by the sulfur p-electrons.[36] Therefore, the photogenerated holes may also be trapped in the bulk crystallite by breaking of this weak Sb−S bond.

$$Sb_2S_3(h) \rightarrow Sb_2S_2S^{-\bullet} \quad (7)$$

As shown in Figure 5B, the growth of the $S^{-\bullet}$ absorption parallels the recovery of the 460 nm bleach peak. This provides further evidence that the process responsible for the fast component of the decay of the 460 nm bleach is also responsible for growth of the 560 nm induced absorption peak. In other words, the decay at 460 nm and growth at 560 nm both arise from the trapping of valence band holes as $S^{-\bullet}$.

Further support for linking the decay of the photobleaching at 460 nm with the growth of the $S^{-\bullet}$ species

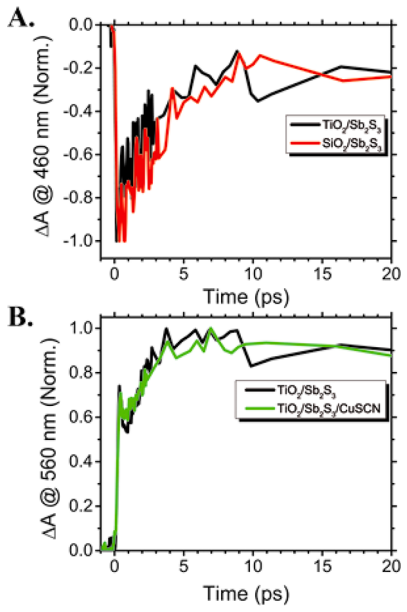

Figure 6. (A) Transient kinetic decay monitored at the 460 nm bleach maximum for Sb_2S_3 films on TiO_2 (black) and SiO_2 (red). Thickness of the Sb_2S_3 film shown in parentheses. (B) Transient kinetic trace showing the rise time of the 560 nm $S^{-\bullet}$ induced absorption peak in the absence and presence of a hole scavenger.

seen at 560 nm was obtained by analyzing SiO_2/Sb_2S_3 and TiO_2/Sb_2S_3 films. The electron transfer pathway is suppressed in SiO_2/Sb_2S_3 films (reaction 4) since the conduction band of SiO_2 is much higher than that of Sb_2S_3 and hence does not accept photoexcited electrons from Sb_2S_3. As shown in Figure 6A, the decay of the 460 nm bleach proceeds at the same rate for Sb_2S_3 films on SiO_2 and TiO_2, showing the dominance of reaction 7 to the bleaching recovery. This also indicates that electron transfer to TiO_2 is not appreciable in the <10 ps time scale as this would be expected to also contribute to the decay of the 460 nm bleach. However, further investigation is needed to fully characterize the electron transfer process from Sb_2S_3 to TiO_2. On the basis of this observation, and the correspondence of this decay with the growth of the $S^{-\bullet}$ absorption at 560 nm (Figure 5B), we attribute the short lifetime (picosecond time scale) of the decay to hole trapping in the Sb_2S_3. The recovery was normalized and fit by a biexponential decay kinetic model shown in eq 8.

$$y = A_1 e^{(-x/\tau_1)} + A_2 e^{(-x/\tau_2)} \quad (8)$$

This fit yielded a short (τ_1) and a long (τ_2) decay lifetime and weighted coefficients (A_1 and A_2) representing the contribution of each exponent to the normalized biexponential. From the fitting parameters, summarized in Table 1, the hole trapping process was found to proceed at a rate of 4.5×10^{11} s^{-1}.

Hole Transfer to CuSCN. The formation of $S^{-\bullet}$, as monitored by the absorption growth at 560 nm, is unaffected by the presence of CuSCN (Figure 6B). This

TABLE 1. Results of Biexponential Fit to 460 nm Bleach Decay of TiO_2/Sb_2S_3 Films

sample	A_1	τ_1 (ps)	A_2	τ_2 (ps)	χ^{2a}	k_{trap} (s^{-1})^b
TiO_2/Sb_2S_3	77.4%	2.20	22.6%	2510	1.12×10^{-2}	4.5×10^{11}

[a] Represents the quality of the fit (fit is best when χ^2 is minimized). [b] The hole trapping rate, k_{trap}, was calculated from the short component of the recovery lifetime, τ_1, by the equation: $k_{trap} = 1/\tau_1$.

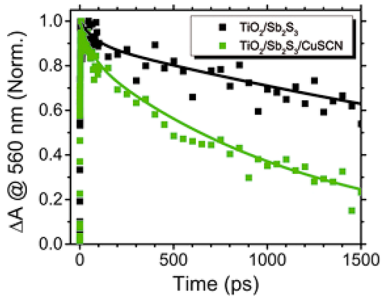

Figure 7. Transient kinetic trace showing the decay and kinetic fits (solid lines) of the 560 nm $S^{-\bullet}$ absorption for a TiO_2/Sb_2S_3 film with and without CuSCN.

TABLE 2. Results of Biexponential Fitting of Induced Absorption Decay at Peak Wavelength

sample	A_1	τ_1 (ps)	A_2	τ_2 (ps)	χ^{2a}	$\langle\tau\rangle$ (ps)^b	k_{ht} (s^{-1})
TiO_2/Sb_2S_3	9.5%	80.9	90.5%	4137	4.99×10^{-3}	4128	
TiO_2/Sb_2S_3/CuSCN	14.8%	62.8	85.2%	1205	1.59×10^{-3}	1195	5.95×10^8

[a] Represents the quality of the fit (fit is best when χ^2 is minimized). [b] Average lifetime $\langle\tau\rangle$ is calculated by the equation: $\langle\tau\rangle = (A_1\tau_1^2 + A_2\tau_2^2)/(A_1\tau_1 + A_2\tau_2)$.

observation in turn indicates that the hole trapping process that occurs in Sb_2S_3 is a faster process than hole transfer from Sb_2S_3 to CuSCN. In the case of SiO_2/Sb_2S_3 and TiO_2/Sb_2S_3 films, the trapped holes (*viz.*, the $S^{-\bullet}$ species) decay through electron–hole recombination (reaction 9). However, in the presence of CuSCN, we expect scavenging of holes trapped within Sb_2S_3 (reaction 10). If indeed such a hole transfer to CuSCN occurs, we should be able to observe a faster induced absorption recovery at 560 nm for Sb_2S_3/CuSCN samples.

$$Sb_2S_2S^{-\bullet} + e \rightarrow Sb_2S_3 + \text{heat} \quad (9)$$

$$Sb_2S_2S^{-\bullet} + CuSCN \rightarrow Sb_2S_3 + CuSCN(h) \quad (10)$$

To investigate hole transfer from Sb_2S_3 to CuSCN, TiO_2/Sb_2S_3 and TiO_2/Sb_2S_3/CuSCN films were excited with a 387 nm laser pulse and time-resolved transient absorption spectra were recorded. The normalized absorption at 560 nm is shown in Figure 7. The decay at 560 nm was analyzed using a biexponential fit. The fitting parameters are summarized in Table 2. These lifetimes are attributed primarily to a convolution of nonradiative electron–hole recombination and hole

transfer (reactions 9 and 10). To deconvolute hole transfer from electron−hole recombination, it is assumed that the only difference in the kinetic behavior between films with and without CuSCN is the addition of the hole transfer pathway in films employing CuSCN, likely a good assumption for Sb_2S_3 as there is no significant shift in the absorption spectra that would indicate an exchange between Sb^{3+} and Cu^{2+} similar to that observed in CdS/CuSCN solar cells.[18] Using the average lifetime of the $S^{-\bullet}$ species with and without CuSCN, the estimated hole transfer rate can be determined using eq 11.

$$k_{ht} = 1/\langle\tau\rangle_{Sb_2S_3/CuSCN} - 1/\langle\tau\rangle_{Sb_2S_3} \quad (11)$$

where k_{ht} is the estimated hole transfer rate, and $\tau_{Sb_2S_3/CuSCN}$ and $\tau_{Sb_2S_3}$ are the average lifetimes of the decay in the presence and absence of CuSCN, respectively. From these measurements, the estimated hole transfer rate constant from the average lifetime of the trapped hole is $5.9 \times 10^8\ s^{-1}$.

In summary, hole transfer from Sb_2S_3 to CuSCN following the band gap excitation follows two-step mechanism as shown in reactions 12 and 13.

$$Sb_2S_3(h) \xrightarrow{k_{trap}} Sb_2S_2S^{-\bullet} \quad (12)$$

$$Sb_2S_2S^{-\bullet} + CuSCN \xrightarrow{k_{ht}} Sb_2S_3 + Cu(SCN^{-\bullet}) \quad (13)$$

In the initial step, photogenerated holes are trapped as $S^{-\bullet}$ in Sb_2S_3 with a rate constant of $k_{trap} = 4.5 \times 10^{11}\ s^{-1}$. This process is characterized by the formation of surface-bound sulfide radical ($S^{-\bullet}$). These holes are subsequently transferred to CuSCN with a rate constant of $k_{ht} = 5.9 \times 10^8\ s^{-1}$. The transient absorption measurements discussed here provide further insight into the hole transfer mechanism in metal chalcogenide/CuSCN-based solar cells.

CONCLUSION

Elucidation of the hole transfer mechanism in TiO_2/Sb_2S_3/CuSCN ETA solar cells provides a better understanding of charge separation and gives guidance for designing new solar cell architectures for higher efficiency devices. It is interesting to note that typical reported electron transfer rates in CdSe-sensitized metal oxide systems are on the order of $10^{10}-10^{11}\ s^{-1}$,[46] 2−3 orders of magnitude faster than the observed hole transfer rate in this study. Similar slower hole transfer was also recorded earlier for CdSe QDs.[39] This kinetic estimate indicates that these Sb_2S_3/CuSCN solar cells suffer from the slow extraction of holes compared to electrons. Such a slow hole transfer would cause a buildup of holes in the absorber species, causing increased recombination at the $TiO_2-Sb_2S_3$ interface. The present study highlights the need to develop two strategies for obtaining higher efficiency TiO_2/Sb_2S_3/CuSCN solar cells: (i) surface modification at the Sb_2S_3−CuSCN interface with a relay molecule or surface treatment opens up the possibility of increasing the rate of hole extraction from Sb_2S_3, and (ii) modification of the $TiO_2-Sb_2S_3$ interface to reduce recombination of electrons in the TiO_2 with holes in the Sb_2S_3. Such strategies represent challenges for the further optimization and increased efficiency of solid-state semiconductor-sensitized solar cells.

EXPERIMENTAL METHODS

Materials. α-Terpinol (Arco Organics, 97+%), antimony chloride ($SbCl_3$, Alfa Aesar, 99%), benzyl alcohol (Alfa Aesar, 99+%), copper(I) thiocyanate (CuSCN, Strem Chemicals, 99%), ethyl cellulose (MP Biomedicals, Inc.), di-*n*-propyl sulfide ($C_6H_{14}S$, Alfa Aesar, 98%), potassium thiocyanate (KSCN, Aldrich, 99%), sodium thiosulfate pentahydrate ($Na_2S_2O_3 \cdot 5H_2O$, Alfa Aesar, 99%), titanium diisopropoxide bis(acetylacetonate) ($[(CH_3)_2CHO]_2Ti(C_6H_7O_2)_2$, Sigma Aldrich, 75 wt % in isopropyl alcohol), and zinc powder (median 6−9 μm, Alfa Aesar, 97.5%) were used without further purification.

Fabrication of Solar Cells. A portion of the fluorine-doped tin oxide (FTO) glass (Pilkington Glass, TEC-7, 2 mm thickness) was masked, and the exposed area was covered with Zn powder. Concentrated HCl was then dripped over the Zn powder to etch the FTO layer beneath. The FTO electrode was then rinsed with water, cleaned in a detergent solution using an ultrasonic bath for 30 min, rinsed with water and ethanol, and heated at 500 °C for 5 min. A compact layer of TiO_2 (~80 nm) was deposited over the FTO layer by spray pyrolysis using a 0.2 M solution of titanium diisopropoxide bis(acetylacetonate) (TAA) in ethanol.[35] A mesoporous TiO_2 layer (~2 μm) was applied on top of the compact TiO_2 layer by screen printing a homemade P25 (Degussa, 25 nm particles) TiO_2 paste. The TiO_2 films were dried at 80 °C for 1 h and sintered at 500 °C for 1 h. The TiO_2 electrodes were then immersed in a 40 mM solution of $TiCl_4$ at 70 °C for 30 min, rinsed with water and ethanol, and sintered at 500 °C for 30 min. Deposition of Sb_2S_3 was performed by chemical bath deposition (CBD).[47] For the bath solution, 650 mg of $SbCl_3$ was dissolved in 3 mL of acetone and mixed with 97 mL of aqueous 0.25 M $Na_2S_2O_3$ at 7 °C. The TiO_2 films were placed face down at an angle in the bath solution, held at 7 °C for 2 h, rinsed with deionized water, and dried with air. The films were then annealed in a nitrogen glovebox for 20 min at 300 °C until they turned to dark brown, crystalline, stibnite. After being annealed, the films were dipped in a 0.5 M solution of KSCN for 5 min, removed, and the excess KSCN was wicked away. CuSCN was deposited on the TiO_2/Sb_2S_3/KSCN films from a 0.05 M solution of CuSCN in di-*n*-propyl sulfide using an automated deposition system similar to the device reported by O'Regan *et al.*[48] The films were placed on a hot plate held at 80 °C, and the CuSCN solution was spread evenly over the film (1.5 × 2 cm) at 20 μL/min to a final volume of 40 μL/cm^2. The films were dried at 80 °C for an additional 5 min. Excess CuSCN was scribed off of the contact areas, and a gold contact (100 nm) was evaporated on top of the CuSCN. Indium was soldered on the working and counter electrodes to provide good electrical contacts. The solar cell active area was masked using black tape, and ImageJ software[49] was used to determine the precise electrode area. A diagram of the completed solar cell is shown in Figure 8. Because of the performance enhancement caused by light soaking,[25] cells were held at open circuit conditions under 100 mW/cm^2 AM 1.5 illumination for 2 h before measurement.

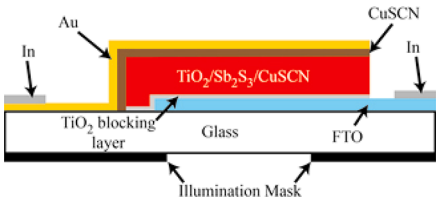

Figure 8. Diagram of TiO_2/Sb_2S_3/CuSCN solar cell.

Preparation of P25 TiO_2 Paste. P25 TiO_2 paste was made similar to previously reported methods.[50] Briefly, ethyl cellulose, benzyl alcohol, α-terpinol, and P25 TiO_2 were used in the following weight ratio: 1:3:18:3.5, respectively. Benzyl alcohol and α-terpinol were added slowly with vigorous stirring at room temperature for ~30 min. The solution was heated to 80 °C, and the ethyl cellulose was slowly added with vigorous stirring for ~30 min. With the solution held at 80 °C, the P25 TiO_2 powder was added slowly with stirring for ~30 min. The paste was then sonicated for 30 min. The resulting white paste was used without further modification for screen-printed TiO_2 electrodes.

Preparation of Sb_2S_3 Films for Transient Absorption Spectroscopy. Glass microscope slides were cleaned in a detergent solution using an ultrasonic bath for 30 min, rinsed with water and ethanol, and heated at 500 °C for 5 min. A ~150 nm compact layer of TiO_2 was deposited by spray pyrolysis. Deposition of antimony sulfide on the compact TiO_2 and cleaned SiO_2 slides was performed by CBD at 7 °C for 30−50 min. The slides were then removed, rinsed with water, and dried with air. The as-deposited films were annealed in a nitrogen glovebox for 20 min at 300 °C until they turned to dark brown, crystalline, stibnite. After annealing, films were stored in dry air until characterization. It should be noted that oxidation of the Sb_2S_3 to form a thin Sb_2O_3 shell has been reported to improve solar cell performance;[26] however, in this study, steps were taken to minimize the formation of this oxide layer. Following characterization of the TiO_2/Sb_2S_3 and SiO_2/Sb_2S_3 films, a CuSCN layer was applied in order to compare the same Sb_2S_3 films with and without CuSCN. Before CuSCN application, the films were dipped in a 0.5 M solution of aqueous KSCN for 5 min. The films were removed, and excess KSCN solution was wicked away. Then approximately 10 μL/cm^2 of 0.05 M CuSCN in di-*n*-propyl sulfide was deposited on the film (0.7 × 2 cm) using the same automated deposition system employed in solar cell fabrication at a rate of 15 μL/min. The completed films were dried at 80 °C for an additional 5 min, removed, and stored in dry air until further characterization.

Optical, Photoelectrochemical, and Structural Characterization. UV−visible absorption spectra were recorded using a Varian Cary 50 Bio spectrophotometer. Photoelectrochemical measurements were carried out using a Princeton Applied Research 2273 (PARstat) potentiostat. A 300 W Xe lamp with an AM 1.5 filter was used to illuminate the solar cells at 100 mW/cm^2. Incident photon to carrier efficiencies (IPCE or external quantum efficiency, EQE) were measured using a Newport Oriel QE/IPCE measurement kit with a silicon photodiode detector. Film cross sections were obtained using an FEI Magellan-400 field emission scanning electron microscope (FESEM).

Femtosecond Transient Absorption. Femtosecond transient absorption measurements were conducted using a Clark MXR 2010 (775 nm, 1 mJ/pulse, fwhm pulse width = 130 fs, 1 kHz repetition rate) and an Ultrafast Systems (Helios) detection system. The fundamental laser output (775 nm) was split into a pump (95%) and a probe (5%). The probe beam passed through an optical delay stage and was focused on a Ti:sapphire crystal to provide a white light continuum. The pump beam was directed through a second harmonic frequency doubler to produce the 387 nm pump beam used in all measurements. The pump was attenuated at 40 μJ/pulse. The optical delay stage provided a probe time window of 1.6 ns with a step resolution of 7 fs. Kinetic traces were assembled at the appropriate wavelengths from the time-resolved data. All films were placed in evacuated quartz cells.

Conflict of Interest: The authors declare no competing financial interest.

Acknowledgment. The research described herein was supported by the Division of Chemical Sciences, Geosciences, and Biosciences, Office of Basic Energy Sciences of the U.S. Department of Energy through Award DE-FC02-04ER15533. This is contribution number NDRL No. 4979 from the Notre Dame Radiation Laboratory.

Supporting Information Available: Figure SI-1 depicts transient absorption spectra for TiO_2/Sb_2S_3, TiO_2/Sb_2S_3/CuSCN, SiO_2/Sb_2S_3, and SiO_2/Sb_2S_3/CuSCN films. Figure SI-2 compares the kinetic decay of the induced absorption peaks seen at 560 and 725 nm. Figure SI-3 shows transient absorption spectra for TiO_2, SiO_2/CuSCN, and TiO_2/CuSCN control films. This material is available free of charge *via* the Internet at http://pubs.acs.org.

Note Added after ASAP Publication: This paper was published ASAP on August 20, 2013. Eq 12 was corrected due to a production error and the revised version was reposted on August 27, 2013.

REFERENCES AND NOTES

1. Kamat, P. V. Quantum Dot Solar Cells. Semiconductor Nanocrystals as Light Harvesters. *J. Phys. Chem. C* **2008**, *112*, 18737–18753.
2. Kamat, P. V. Quantum Dot Solar Cells. *The Next Big Thing* in Photovoltaics. *J. Phys. Chem. Lett.* **2013**, *4*, 908–918.
3. Grätzel, M. Photovoltaic and Photoelectrochemical Conversion of Solar Energy. *Philos. Trans. R. Soc. A* **2007**, *365*, 993–1005.
4. Grätzel, M. Photoelectrochemical Cells. *Nature* **2001**, *414*, 338–344.
5. Genovese, M. P.; Lightcap, I. V.; Kamat, P. V. Sun-Believable Solar Paint. A Transformative One-Step Approach for Designing Nanocrystalline Solar Cells. *ACS Nano* **2012**, *6*, 865–872.
6. Kamat, P. V. Meeting the Clean Energy Demand: Nanostructure Architectures for Solar Energy Conversion. *J. Phys. Chem. C* **2007**, *111*, 2834–2860.
7. Grätzel, M. Photovoltaic Performance and Long-Term Stability of Dye-Sensitized Meosocopic Solar Cells. *C. R. Chim.* **2006**, *9*, 578–583.
8. Li, B.; Wang, L.; Kang, B.; Wang, P.; Qiu, Y. Review of Recent Progress in Solid-State Dye-Sensitized Solar Cells. *Sol. Energy Mater. Sol. Cells* **2006**, *90*, 549–573.
9. Boix, P. P.; Larramona, G.; Jacob, A.; Delatouche, B.; Mora-Seró, I.; Bisquert, J. Hole Transport and Recombination in All-Solid Sb_2S_3-Sensitized TiO_2 Solar Cells Using CuSCN as Hole Transporter. *J. Phys. Chem. C* **2012**, *116*, 1579–1587.
10. Hodes, G.; Cahen, D. All-Solid-State, Semiconductor-Sensitized Nanoporous Solar Cells. *Acc. Chem. Res.* **2012**, *45*, 705–713.
11. Green, M. A.; Emery, K.; Hishikawa, Y.; Warta, W.; Dunlop, E. D. Solar Cell Efficiency Tables (version 40). *Prog. Photovoltaics* **2012**, *20*, 606–614.
12. Kongkanand, A.; Tvrdy, K.; Takechi, K.; Kuno, M.; Kamat, P. V. Quantum Dot Solar Cells. Tuning Photoresponse through Size and Shape Control of CdSe−TiO_2 Architecture. *J. Am. Chem. Soc.* **2008**, *130*, 4007–4015.
13. Hanewinkel, B.; Knorr, A.; Thomas, P.; Koch, S. W. Optical Near-Field Response of Semiconductor Quantum Dots. *Phys. Rev. B* **1997**, *55*, 13715–13725.
14. Yu, W. W.; Qu, L.; Guo, W.; Peng, X. Experimental Determination of the Extinction Coefficient of CdTe, CdSe, and CdS Nanocrystals. *Chem. Mater.* **2003**, *15*, 2854–2860.
15. Ross, R. T. Efficiency of Hot-Carrier Solar Energy Converters. *J. Appl. Phys.* **1982**, *53*, 3813–3818.
16. Ellingson, R. J.; Beard, M. C.; Johnson, J. C.; Yu, P.; Micic, O. I.; Nozik, A. J.; Shabaev, A.; Efros, A. L. Highly Efficient Multiple Exciton Generation in Colloidal PbSe and PbS Quantum Dots. *Nano Lett.* **2005**, *5*, 865–871.

17. Schaller, R. D.; Klimov, V. I. High Efficiency Carrier Multiplication in PbSe Nanocrystals: Implications for Solar Energy Conversion. *Phys. Rev. Lett.* **2004**, *92*, 1–4.
18. Larramona, G.; Choné, C.; Jacob, A.; Sakakura, D.; Delatouche, B.; Péré, D.; Cieren, X.; Nagino, M.; Bayón, R. Nanostructured Photovoltaic Cell of the Type Titanium Dioxide, Cadmium Sulfide Thin Coating, and Copper Thiocyanate Showing High Quantum Efficiency. *Chem. Mater.* **2006**, *18*, 1688–1696.
19. Lévy-Clément, C.; Tena-Zaera, R.; Ryan, M. A.; Katty, A.; Hodes, G. CdSe-Sensitized p-CuSCN/Nanowire n-ZnO Heterojunctions. *Adv. Mater.* **2005**, *17*, 1512–1515.
20. Mora-Seró, I.; Giménez, S.; Fabregat-Santiago, F.; Azaceta, E.; Tena-Zaera, R.; Bisquert, J. Modeling and Characterization of Extremely Thin Absorber (ETA) Solar Cells Based on ZnO Nanowires. *Phys. Chem. Chem. Phys.* **2011**, *13*, 7162–7169.
21. Zou, Y.; Li, D.; Sheng, X.; Wang, L.; Yang, D. Fabrication of TiO_2 Nanorod Array/Semiconductor Nanocrystal Hybrid Structure for Photovoltaic Applications. *Sol. Energy* **2012**, *86*, 1359–1365.
22. Belaidi, A.; Dittrich, T.; Kieven, D.; Tornow, J.; Schwarzburg, K.; Lux-Steiner, M. Influence of the Local Absorber Layer Thickness on the Performance of ZnO Nanorod Solar Cells. *Phys. Status Solidi (RRL)* **2008**, *2*, 172–174.
23. Chang, J. A.; Im, S. H.; Lee, Y. H.; Kim, H.-J.; Lim, C.-S.; Heo, J. H.; Il Seok, S. Panchromatic Photon-Harvesting by Hole-Conducting Materials in Inorganic−Organic Heterojunction Sensitized-Solar Cell through the Formation of Nanostructured Electron Channels. *Nano Lett.* **2012**, *12*, 1863–1867.
24. Boix, P. P.; Lee, Y. H.; Fabregat-Santiago, F.; Im, S. H.; Mora-Sero, I.; Bisquert, J.; Il Seok, S. From Flat to Nanostructured Photovoltaics: Balance between Thickness of the Absorber and Charge Screening in Sensitized Solar Cells. *ACS Nano* **2012**, *6*, 873–880.
25. Nezu, S.; Larramona, G.; Choné, C.; Jacob, A.; Delatouche, B.; Péré, D.; Moisan, C. Light Soaking and Gas Effect on Nanocrystalline TiO_2/Sb_2S_3/CuSCN Photovoltaic Cells Following Extremely Thin Absorber Concept. *J. Phys. Chem. C* **2010**, *114*, 6854–6859.
26. Itzhaik, Y.; Niitsoo, O.; Page, M.; Hodes, G. Sb_2S_3-Sensitized Nanoporous TiO_2 Solar Cells. *J. Phys. Chem. C* **2009**, *113*, 4254–4256.
27. Moon, S.-J.; Itzhaik, Y.; Yum, J.-H.; Zakeeruddin, S. M.; Hodes, G.; Grätzel, M. Sb_2S_3-Based Mesoscopic Solar Cell Using an Organic Hole Conductor. *J. Phys. Chem. Lett.* **2010**, *1*, 1524–1527.
28. Tsujimoto, K.; Nguyen, D.; Ito, S.; Nishino, H.; Matsuyoshi, H.; Konno, A.; Kumara, G. R. A.; Tennakone, K. TiO_2 Surface Treatment Effects by Mg^{2+}, Ba^{2+}, and Al^{3+} on Sb_2S_3 Extremely Thin Absorber Solar Cells. *J. Phys. Chem. C* **2012**, *116*, 13465–13471.
29. Chang, J. A.; Rhee, J. H.; Im, S. H.; Lee, Y. H.; Kim, H.; Il Seok, S.; Nazeeruddin, M. K.; Gratzel, M. High-Performance Nanostructured Inorganic−Organic Heterojunction Solar Cells. *Nano Lett.* **2010**, *10*, 2609–2612.
30. Fujita, T.; Kurita, K.; Takiyama, K.; Oda, T. The Fundamental Absorption Edge and Electronic Structure in Sb_2S_3. *J. Phys. Soc. Jpn.* **1987**, *56*, 3734–3739.
31. Rost, C.; Sieber, I.; Fischer, C.; Lux-Steiner, M. C.; Könenkamp, R. Semiconductor Growth on Porous Substrates. *Mater. Sci. Eng., B* **2000**, *69−70*, 570–573.
32. O'Mahony, F. T. F.; Lutz, T.; Guijarro, N.; Gómez, R.; Haque, S. A. Electron and Hole Transfer at Metal Oxide/Sb_2S_3/spiro-OMeTAD Heterojunctions. *Energy Environ. Sci* **2012**, *5*, 9760–9764.
33. Bansal, N.; O'Mahony, F. T. F.; Lutz, T.; Haque, S. A. Solution Processed Polymer-Inorganic Semiconductor Solar Cells Employing Sb_2S_3 as a Light Harvesting and Electron Transporting Material. *Adv. Energy Mater.* **2013**, *8*, 986–990.
34. Guijarro, N.; Lutz, T.; Lana-Villarreal, T.; O'Mahony, F.; Gómez, R.; Haque, S. A. Toward Antimony Selenide Sensitized Solar Cells: Efficient Charge Photogeneration at spiro-OMeTAD/Sb_2Se_3/Metal Oxide Heterojunctions. *J. Phys. Chem. Lett.* **2012**, *3*, 1351–1356.
35. Kavan, L.; Grätzel, M. Highly Efficient Semiconducting TiO_2 Photoelectrodes Prepared by Aerosol Pyrolysis. *Electrochim. Acta* **1995**, *40*, 643–652.
36. Ghosh, C.; Varma, B. P. Optical Properties of Amorphous and Crystalline Sb_2S_3 Thin Films. *Thin Solid Films* **1979**, *60*, 61–65.
37. Versavel, M. Y.; Haber, J. A. Structural and Optical Properties of Amorphous and Crystalline Antimony Sulfide Thin-Films. *Thin Solid Films* **2007**, *515*, 7171–7176.
38. Itzhaik, Y.; Hodes, G.; Cohen, H. Band Alignment and Internal Field Mapping in Solar Cells. *J. Phys. Chem. Lett.* **2011**, *2*, 2872–2876.
39. Chakrapani, V.; Baker, D. R.; Kamat, P. V. Understanding the Role of the Sulfide Redox Couple (S^{2-}/S_n^{2-}) in Quantum Dot-Sensitized Solar Cells. *J. Am. Chem. Soc.* **2011**, *133*, 9607–9615.
40. Baral, S.; Fojtik, A.; Weller, H.; Henglein, A. Photochemistry and Radiation Chemistry of Colloidal Semiconductors. 12. Intermediates of the Oxidation of Extremely Small Particles of Cadmium Sulfide, Zinc Sulfide, and Tricadmium Diphosphide and Size Quantization Effects (A Pulse Radiolysis Study). *J. Am. Chem. Soc.* **1986**, *108*, 375–378.
41. Kamat, P. V.; Dimitrijevic, N. M.; Fessenden, R. W. Photoelectrochemistry in Particulate Systems. 6. Electron-Transfer Reactions of Small Cadmium Sulfide Colloids in Acetonitrile. *J. Phys. Chem.* **1987**, *91*, 396–401.
42. Haase, M.; Weller, H.; Henglein, A. Photochemistry of Colloidal Semiconductors. 26. Photoelectron Emission from Cadmium Sulfide Particles and Related Chemical Effects. *J. Phys. Chem.* **1988**, *92*, 4706–4712.
43. Kamat, P. V; Dimitrijevic, N. M.; Fessenden, R. W. Photoelectrochemistry in Particulate Systems. 7. Electron-Transfer Reactions of Indium Sulfide Semiconductor Colloids. *J. Phys. Chem.* **1988**, *92*, 2324–2329.
44. Kamat, P. V.; Ebbesen, T. W.; Dimitrijević, N. M.; Nozik, A. J. Primary Photochemical Events in CdS Semiconductor Colloids as Probed by Picosecond Laser Flash Photolysis. *Chem. Phys. Lett.* **1989**, *157*, 384–389.
45. Zhang, J. Z. Interfacial Charge Carrier Dynamics of Colloidal Semiconductor Nanoparticles. *J. Phys. Chem. B* **2000**, *104*, 7239–7253.
46. Tvrdy, K.; Frantsuzov, P. A.; Kamat, P. V. Photoinduced Electron Transfer from Semiconductor Quantum Dots to Metal Oxide Nanoparticles. *Proc. Natl. Acad. Sci. U.S.A.* **2011**, *108*, 29–34.
47. Nair, M. T. S.; Peña, Y.; Campos, J.; Garcia, V. M.; Nair, P. K. Chemically Deposited Sb_2S_3 and Sb_2S_3-CuS Thin Films. *J. Electrochem. Soc.* **1998**, *145*, 2113–2120.
48. O'Regan, B. C.; Lenzmann, F. Charge Transport and Recombination in a Nanoscale Interpenetrating Network of n-Type and p-Type Semiconductors: Transient Photocurrent and Photovoltage Studies of TiO_2/Dye/CuSCN Photovoltaic Cells. *J. Phys. Chem. B* **2004**, *108*, 4342–4350.
49. Schneider, C. A.; Rasband, W. S.; Eliceiri, K. W. NIH Image to ImageJ: 25 Years of Image Analysis. *Nat. Methods* **2012**, *9*, 671–675.
50. Knodler, R.; Sopka, J.; Harbach, F.; Griinling, H. W. Photoelectrochemical Cells Based on Dye Sensitized Colloidal TiO_2 Layers. *Sol. Energy Mater. Sol. Cells* **1993**, *30*, 277–281.